Phase-Constrained Reconstruction of High-Resolution Multi-shot Diffusion Weighted Image

Yiman Huang[1], Xinlin Zhang[1], Hua Guo[2], Huijun Chen[2], Di Guo[3], Feng Huang[4], Qin Xu[4], Xiaobo Qu[1*]

[1] Department of Electronic Science, Fujian Provincial Key Laboratory of Plasma and Magnetic Resonance, School of Electronic Science and Engineering, Xiamen University, Xiamen 361005, China.

[2] Center for Biomedical Imaging Research, Department of Biomedical Engineering, Tsinghua University, Beijing, 100084, China.

[3] School of Computer and Information Engineering, Fujian Provincial University Key Laboratory of Internet of Things Application Technology, Xiamen University of Technology, Xiamen 361024, China.

[4] Neusoft Medical System, Shanghai 200241, China.

Abstract

Diffusion weighted imaging (DWI) is a unique examining method in tumor diagnosis, acute stroke evaluation. Single-shot echo planar imaging is currently conventional method for DWI. However, single-shot DWI suffers from image distortion, blurring and low spatial resolution. Although multi-shot DWI improves image resolution, it brings phase variations among different shots at the same time. In this paper, we introduce a smooth phase constraint of each shot image into multi-shot navigator-free DWI reconstruction by imposing the low-rankness of Hankel matrix constructed from the k-space data. Furthermore, we exploit the partial sum minimization of singular values to constrain the low-rankness of Hankel matrix. Results on brain imaging data show that the proposed method outperforms the state-of-the-art methods in terms of artifacts removal and our method potentially has the ability to reconstruct high number of shot of DWI.

Key Words: Diffusion weighted imaging, Hankel matrix, image reconstruction, low-rankness, magnetic resonance imaging.

[*] Corresponding to: Xiaobo Qu, Department of Electronic Science, Xiamen University, Xiamen 361005, China (email: quxiaobo@xmu.edu.cn).

1. Introduction

Diffusion weighted magnetic resonance imaging (MRI) is a unique examining method noninvasively detecting the Brownian motion of water molecules in the tissues in biomedical imaging [1, 2]. It is widely used in tumor diagnosis, acute stroke evaluation and neuroscience research [3-5]. As a conventional method of diffusion weighted imaging (DWI) acquisition, single-shot echo-planar imaging (EPI) has the advantages of motion immunity and short acquisition time, but suffers from image distortion, blurring and low spatial resolution [6]. some methods were proposed to overcome the distortion in DWI, such as spatiotemporal encoding [7] and multi-shot EPI.

The multi-shot interleaved EPI fully acquires the k-space data by sampling different segment in each shot, as shown in Figure 1. Multi-shot EPI provides higher spatial resolution than single-shot EPI. However, multi-shot EPI is sensitive to physiological motions, which will induce phase variations from shot to shot. Directly interleaving multi-shot data together into fully sampled k-space will lead to severe artifacts in image.

Many methods have been proposed to correct phase variations among multiple shots to obtain artifact-free DWI images [8-13]. For example, some methods explore navigator signals to correct phase variations, assuming that the navigator signal shares the same phase variation with image signal in each shot. Therefore, the navigator signals can be adopted to estimate phase variation for image reconstruction [8, 14] or as auto-calibrated signals for calibration kernel estimation [9, 15]. However, these navigator-based methods need additional scan time to acquire these navigators and there may be mismatches between target images and navigators [16]. In comparison, mismatch is not a problem for navigator-free reconstruction methods [10-13], which had shown exciting performance in brain imaging. Multiplexed sensitivity encoding (MUSE) [10] is a typical navigator-free reconstruction method, which used two step sensitivity encoding (SENSE) [17] parallel imaging reconstruction. MUSE relied on the performance of the first step SENSE reconstruction. When the number of shots getting higher, the first SENSE reconstruction would not be good, which affects the accuracy of phase variation. The projections onto convex sets enhanced inherent correction of motion-induced phase errors (POCS-ICE) [11] is another typical method for navigator-free reconstruction, which update the phase errors through iterative reconstruction.

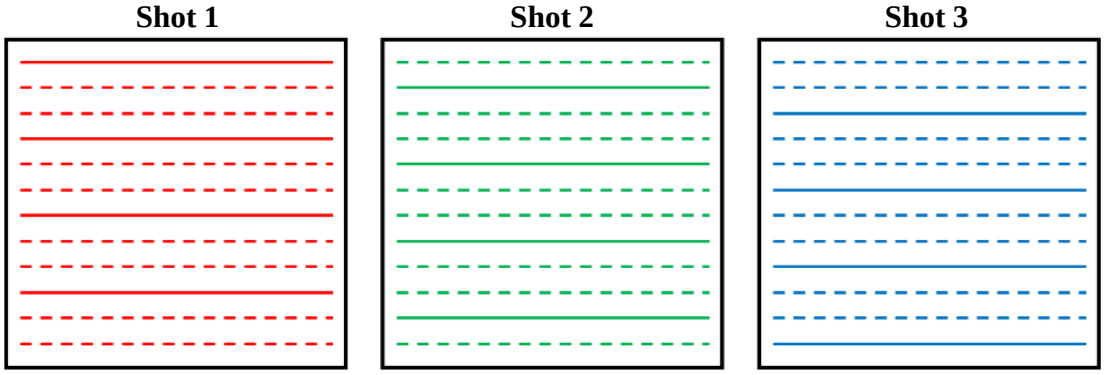

Figure 1. A schematic diagram of 3-shot interleaved DWI. Note: The solid lines represent the collecting lines in the k-space (Fourier space) of images, and the dotted lines denote the lines where signals are not sampled.

Recently, many low-rank Hankel matrix (LRHM) completion methods have been exploited to reconstruct magnetic resonance images [18-22] and spectrum [23-27]. The low-rank Hankel matrix depends on the linear correlations among the Fourier coefficients, which arose from the continuous domain analogs of sparsity [20, 21, 28], correlations in multi-channel [29-31] , smooth phase property in spatial domain [19] or the spatiotemporal properties [32-34] in cardiac imaging, dynamic contrast-enhanced imaging, etc..

Some researchers exploited the correlation of different shots and the LRHM completion methods to recover multi-shot DWI images [12, 13], and achieved promising reconstructions. Multi-shot sensitivity encoded diffusion data recovery using structured low-rank matrix completion (MUSSELS) [12] combines the multi-channel images by SENSE scheme and concatenates low-rank Hankel matrix constructed shot by shot under the assumption that the additional phase of each shot DW image is support limited in k-space. Low-rank modeling of local k-space neighborhood (LORAKS) [19] is a representative LRHM method that constrains the compact support of image or the smooth phase property. One LORAKS-based method was proposed for navigator-free EPI ghost correction [35]. The paper mentions that the method would effectively adapt to multi-shot EPI imaging by concatenating multi-shot and multi-channel data without SENSE reconstruction. However, the size of constructed Hankel matrix would be very large as the number of channels and shots getting higher. One difference between the proposed method and MUSSELS is that the strategies of Hankel matrix construction are different even though the basic signal assumptions are similar. The Hankel matrix construction of the proposed method is based on the LORAKS **S**-matrix while MUSSELS constructs the block Hankel matrix. Another difference is MUSSELS exploits the convex nuclear norm to constrain the low-rankness of block Hankel matrix and the proposed method utilizes the non-convex optimization followed by partial sum of singular values thresholding operator. A major difference between the proposed approach and [35] is that [35] concatenates the multi-shot and multi-channel LORAKS **S**-matrices while the proposed method concatenates the Hankel matrix of composed image from multi-channel images. Another difference is [35] utilizes the

Frobenius norm to encourage the low-rank property and the proposed method constrains the partial sum of singular values of Hankel matrix.

In this work, we propose a reconstruction method for multi-shot DWI that utilizes the low-rank property derived from the smooth phase of each shot image. The proposed method imposes the low-rankness of Hankel matrix constructed from multi-shot k-space data, and combines the sensitivity encoding strategy [17] which performs well in uniformly under-sampled parallel imaging. In addition, we adopt the partial singular value thresholding strategy to further strengthen the low-rankness constraint. Numerical simulation and *in vivo* experiments show that our approach has the capability to provide reconstruction with less artifacts, sharper images in accelerated DWI.

2. Theory

S-based LORAKS [19] constrains the smooth phase of MRI, and is powerful in MRI reconstruction. A complex value image $\boldsymbol{\rho}$ can be decomposed into magnitude $\mathbf{m}$ and phase $\phi = \angle\boldsymbol{\rho}$, let $\mathbf{h} = e^{j\phi}$ such that

$$\boldsymbol{\rho}=\mathbf{m}\cdot\mathbf{h}. \tag{1}$$

It is observed that

$$\boldsymbol{\rho}\cdot\mathbf{h}^{*}=\boldsymbol{\rho}^{*}\cdot\mathbf{h}, \tag{2}$$

where superscript $*$ denotes complex conjugation, $\cdot$ the dot product.

Assuming that $\mathbf{h}$ and $\mathbf{h}^{*}$ are slowly spatial varying or so called smooth, the Fourier domain of $\mathbf{h}$ and $\mathbf{h}^{*}$ would have limited support. We use a radius-R circle region to approximate the kernel. Applying Fourier transform on Eq.(2), and with the convolution theorem of Fourier transform, one can obtain the following relationship:

$$\boldsymbol{\rho}\otimes\mathbf{h}^{*}=\boldsymbol{\rho}^{*}\otimes\mathbf{h}, \tag{3}$$

where $\boldsymbol{\rho}$ and $\mathbf{h}$ are the Fourier transform of $\boldsymbol{\rho}$ and $\mathbf{h}$, respectively; $\otimes$ is the convolution symbol. Rewrite Eq. (3) into a multiplicative form:

$$\sum_{(p,q)\in\mathbb{Z}^2}\boldsymbol{\rho}\left[n_x-p,n_y-q\right]\mathbf{h}^{*}[p,q]=\sum_{(p,q)\in\mathbb{Z}^2}\boldsymbol{\rho}^{*}\left[-n_x-p,-n_y-q\right]\mathbf{h}[p,q], \tag{4}$$

where $\mathbb{Z}^2$ is the approximated radius-R circle kernel region with N_R elements. Extracting the real and imaginary part separately from Eq.(4), we can easily deduce the following relationships:

$$\begin{aligned}&\sum_{(p,q)\in\Lambda_R}\boldsymbol{\rho}_r\left[n_x-p,n_y-q\right]\mathbf{h}_r[p,q]+\sum_{(p,q)\in\Lambda_R}\boldsymbol{\rho}_i\left[n_x-p,n_y-q\right]\mathbf{h}_i[p,q]-\\&\sum_{(p,q)\in\Lambda_R}\boldsymbol{\rho}_r\left[-n_x-p,-n_y-q\right]\mathbf{h}_r[p,q]-\sum_{(p,q)\in\Lambda_R}\boldsymbol{\rho}_i\left[-n_x-p,-n_y-q\right]\mathbf{h}_i[p,q]\approx 0,\end{aligned} \tag{5}$$

$$\begin{aligned}&\sum_{(p,q)\in\Lambda_R}\boldsymbol{\rho}_i\left[n_x-p,n_y-q\right]\mathbf{h}_r[p,q]-\sum_{(p,q)\in\Lambda_R}\boldsymbol{\rho}_r\left[n_x-p,n_y-q\right]\mathbf{h}_i[p,q]+\\&\sum_{(p,q)\in\Lambda_R}\boldsymbol{\rho}_i\left[-n_x-p,-n_y-q\right]\mathbf{h}_r[p,q]-\sum_{(p,q)\in\Lambda_R}\boldsymbol{\rho}_r\left[-n_x-p,-n_y-q\right]\mathbf{h}_i[p,q]\approx 0.\end{aligned} \tag{6}$$

where the subscript r and i represent the real and imaginary part of $\boldsymbol{\rho}$ and $\mathbf{h}$, respectively. We further define four matrices $\mathbf{S}_{r+},\mathbf{S}_{r-},\mathbf{S}_{i+},\mathbf{S}_{i-}$ which respectively have elements:

$$\begin{aligned}\mathbf{S}_{r+}[l,m]&=\boldsymbol{\rho}_r[\ n_x^{(l)}-p_m,\ \ n_y^{(l)}-q_m],\ \mathbf{S}_{r-}[l,m]=\boldsymbol{\rho}_r[-n_x^{(l)}-p_m,-n_y^{(l)}-q_m]\\ \mathbf{S}_{i+}[l,m]&=\boldsymbol{\rho}_i[\ n_x^{(l)}-p_m,\ \ n_y^{(l)}-q_m],\ \mathbf{S}_{i-}[l,m]=\boldsymbol{\rho}_i[-n_x^{(l)}-p_m,-n_y^{(l)}-q_m]\end{aligned} \tag{7}$$

for $l=1,...,L$, $L=(N_1-2R)(N_2-2R)$ and $m=1,...,N_R$. Let $\mathbf{h}_r$ and $\mathbf{h}_i$ denote the vectorized $\mathbf{h}_r$ and $\mathbf{h}_i$. We can rewrite the Eq. (5) and Eq. (6) into matrix multiplication form:

$$\left(\mathcal{P}_S\boldsymbol{\rho}\right)\mathbf{h}=\mathbf{S}\begin{bmatrix}\mathbf{h}_r\\ \mathbf{h}_i\end{bmatrix}=\begin{bmatrix}\mathbf{S}_{r+}-\mathbf{S}_{r-} & \mathbf{S}_{i+}-\mathbf{S}_{i-}\\ \mathbf{S}_{i+}+\mathbf{S}_{i-} & -\mathbf{S}_{r+}-\mathbf{S}_{r-}\end{bmatrix}\begin{bmatrix}\mathbf{h}_r\\ \mathbf{h}_i\end{bmatrix}\approx\mathbf{0}, \tag{8}$$

where $\mathcal{P}_S:\mathbb{C}^{N_1\times N_2}\to\mathbb{R}^{2L\times 2N_R}$ is an operator that converts a complex matrix with size $N_1\times N_2$ into Hankel matrix.

The annihilating relationship in Eq. (8) implies that the matrix $\mathbf{S}$ potentially has null-space thus low-rank characteristic can be utilized in MRI image reconstruction.

3. Methods

3.1 Proposed method

In multi-shot DWI acquisition, each shot of k-space data is sampled in a uniform manner (Figure 1). Some methods consider the DWI reconstruction as sensitivity encoding reconstruction by extending different shots as virtual channels. However, the important phase information may be inaccurately estimated, resulting in sub-optimal reconstruction results. In order to avoid the difficulty in phase estimation, we tend to reconstruct each shot image rather than directly reconstruct a combined DWI image from multi-shots.

While each shot image possesses smooth phase property [11, 36] (a toy example is shown in Figure 2(a)), the concatenated Hankel matrix of shots would have a better low-rank characteristic than one shot. (Figure 2(b)). Our method is to constrain the rank of phase-constrained low-rank Hankel matrix (PLRHM) and it can be formulated as rank minimization problem:

$$\text{minimize rank}(\mathcal{P}_s\mathbf{X})\ \text{ s. t. }\ \mathbf{Y}_i=\mathcal{U}\mathcal{F}\mathbf{C}_i\mathcal{F}^{-1}\mathbf{X}+\boldsymbol{\eta} \tag{9}$$

where $\mathbf{X}=[\mathbf{x}_1,..,\mathbf{x}_N]$ denotes concatenated matrices of k-space data of shots, $\mathcal{P}_s\mathbf{X}=[\mathcal{P}_s\mathbf{x}_1,...,\mathcal{P}_s\mathbf{x}_k,...,\mathcal{P}_s\mathbf{x}_N]$, $\mathcal{P}_s$ is an operator that converts $\mathbf{x}_k$ into so called $\mathbf{S}$-matrix as described in last section, $\mathcal{F}$ the Fourier transform operator, $\mathcal{F}^{-1}$ the inverse Fourier transform operator, $\mathbf{C}_i$ the i^{th} channel coil sensitivity map, $\mathcal{U}$ an operator that under-samples k-space data and zero-fills the non-sampled data points, $\mathbf{Y}_i$ the i^{th} channel sampled k-space data, $\boldsymbol{\eta}$ denotes the measurement noise.

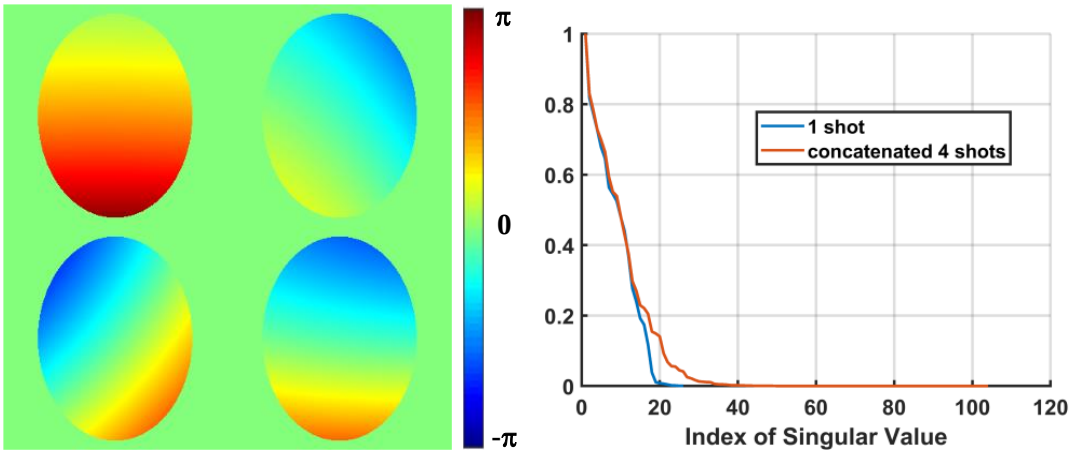

(a) (b)

Figure 2. Example of smooth phase and its low rankness in the k-space. (a) a simulated 4-shot smooth phases, (b) the singular values of the Hankel matrix concatenated from the k-space of four shots in (a) according to $\mathcal{P}_s$ in Eq. (9).

Theoretical studies show that the nuclear norm is the tightest convex lower bound of the rank-minimum problem [37], and many methods have been proposed to solve the nuclear norm optimization problem. However, they may lead to sub-optimal performance, and some researches try to minimize the partial sum of singular values [38, 39]. In this paper, we exploit the partial sum of singular values to constrain low-rankness, therefore, our proposed rank minimization model in Eq. (9) is revised as:

$$\text{(PLRHM)}\quad \min_{\mathbf{X}} \frac{\lambda}{2}\sum_{i}^{I}\| \mathbf{Y}_i - \mathcal{U}\mathcal{F}\mathbf{C}_i\mathcal{F}^{-1}\mathbf{X}\|_F^2 + \sum_{i=r+1}^{\min(m,n)} \sigma_i(\mathcal{P}_s\mathbf{X}), \tag{10}$$

where r is the rank of $\mathcal{P}_s\mathbf{X}$, m,n the matrix size of $\mathcal{P}_s\mathbf{X}$, λ a regularization parameter that balances the data consistency and low-rankness constraint.

3.2 Numerical algorithm

Here, we utilize the alternating direction method of multiplier (ADMM) [23, 25-27, 40] to deal with the proposed model in Eq. (10). The augmented Lagrangian of Eq. (10) is

$$\max_{\mathbf{D}} \min_{\mathbf{X},\mathbf{Z}} \frac{\lambda}{2}\sum_{i}^{I}\| \mathbf{Y}_i - \mathcal{U}\mathcal{F}\mathbf{C}_i\mathcal{F}^{-1}\mathbf{X}\|_F^2 + \sum_{i=r+1}^{\min(m,n)} \sigma_i(\mathbf{Z}) + \Re\mathfrak{e} < \mathbf{D}, \mathcal{P}_s\mathbf{X} - \mathbf{Z} > + \frac{\rho}{2}\| \mathcal{P}_s\mathbf{X} - \mathbf{Z}\|_F^2, \tag{11}$$

where $\mathbf{D}$ denotes the Lagrangian multiplier, $<\cdot,\cdot>$ the inner product in the Hilbert space of complex matrices, $\Re\mathfrak{e}$ denotes the real part of a complex value, ρ the penalty parameter, $\mathbf{Z}$ the auxiliary variable. The solution can be obtained by alternatively solving the sub-problems:

$$\mathbf{Z}^{(k+1)} = \arg\min_{\mathbf{Z}} \sum_{i=r+1}^{\min(m,n)} \sigma_i(\mathbf{Z}) + \frac{\rho}{2}\| \mathcal{P}_s\mathbf{X}^{(k+1)} - \mathbf{Z}^{(k)} + \frac{\mathbf{D}^{(k)}}{\rho}\|_F^2, \tag{12}$$

$$\mathbf{X}^{(k+1)} = \arg\min_{\mathbf{X}} \frac{\lambda}{2}\sum_i \| \mathbf{Y}_i - \mathcal{U}\mathcal{F}\mathbf{C}_i\mathcal{F}^{-1}\mathbf{X}^{(k)} \|_F^2 + \frac{\rho}{2}\| \mathcal{P}_s\mathbf{X}^{(k)} - \mathbf{Z}^{(k)} + \frac{\mathbf{D}^{(k)}}{\rho} \|_F^2, \tag{13}$$

$$\mathbf{D}^{(k+1)} = \mathbf{D}^{(k)} + \tau(\mathcal{P}_s\mathbf{X}^{(k+1)} - \mathbf{Z}^{(k+1)}), \tag{14}$$

where τ is the step size and is set as 1 in each iteration.

To minimize Eq.(12), we adopt partial singular value thresholding (PSVT) [39] scheme which has better performance in rank constraint.

For fixed $\mathbf{X}^{(k+1)}$ and $\mathbf{D}^{(k)}$, $\mathbf{Z}^{(k+1)}$ can be solved by

$$\mathbf{Z}^{(k+1)} = \mathbb{P}_{r,1/\rho}(\mathcal{P}_s\mathbf{X}^{(k+1)} + \frac{\mathbf{D}^{(k)}}{\rho}), \tag{15}$$

where $\mathbb{P}_{r,1/\rho}(\mathbf{A}) = \mathbf{U}(\Sigma_1 + \mathcal{S}_{1/\rho}(\Sigma_2))\mathbf{V}^H = \mathbf{Y}_1 + \mathbf{U}\mathcal{S}_{1/\rho}(\Sigma_2)\mathbf{V}^H$, $\mathbf{A} = \mathbf{U}(\Sigma_1 + \Sigma_2)\mathbf{V}^H$ is the singular value decomposition, $\Sigma_1 = diag(\sigma_1,...,\sigma_r,0,...0)$ and $\Sigma_2 = diag(0,...,0,\sigma_{r+1},...,\sigma_N)$ are the first r and the last $N-r$ singular values, respectively, $\mathcal{S}_p(x) = \frac{x}{|x|}\max(|x|-p,0)$ is soft-thresholding operator. For fixed $\mathbf{Z}^{(k)}$ and $\mathbf{D}^{(k)}$, $\mathbf{X}^{(k+1)}$ has a close-form solution as

$$\mathbf{X} = (\lambda\sum_i^I \mathcal{F}\mathbf{C}_i^*\mathcal{F}^{-1}\mathbf{U}^T\mathbf{U}\mathcal{F}\mathbf{C}_i\mathcal{F}^{-1} + \rho\mathcal{P}_s^*\mathcal{P}_s)^{-1}(\lambda\sum_i \mathcal{F}\mathbf{C}_i^*\mathcal{F}^*\mathbf{U}^T\mathbf{Y}_i + \rho\mathcal{P}_s^*\mathbf{Z}^{(k)} - \mathcal{P}_s^*\mathbf{D}^{(k)}). \tag{16}$$

The numerical algorithm is summarized in Algorithm 1.

Algorithm 1 Multi-shot DWI reconstruction with PLRHM

Input: $\mathbf{Y}, \mathbf{U}, \mathbf{S}, \lambda, \rho, \tau, r$.

Initialization: $\mathbf{Z}$ is initialized as random matrix, $\mathbf{D}_1$=**1**, $k = 1$.

Output: $\mathbf{X}$.

1: **while** $k \le 100$ and $\| \mathbf{X}^{(k+1)} - \mathbf{X}^{(k)} \|_F^2 / \| \mathbf{X}^{(k)} \|_F^2 \ge 10^{-6}$ **do**

2: Update $\mathbf{Z}$ by solving Eq.(15);
3: Update $\mathbf{X}$ by solving Eq.(16);
4: Update $\mathbf{D}$ by solving Eq.(14);
5: $k = k + 1$;
6: **end while**

3.3 Computational complexity

The original optimal problem in Eq. (10) is solved by the alternating direction method of multipliers (ADMM). With variable splitting strategy, the solution can be obtained by iteratively solving a partial sum of singular minimization problem and a linear least-square problem. The least-square problem in Eq. (13) can be solved using conjugate gradient method in $\mathcal{O}(N^3)$ operations [41], where N is the length of the unknown variable in the linear least-square problem. The partial sum of singular minimization problem in Eq. (15) can be minimized by partial sum of singular value thresholding operator [39] where SVD computation occupies the largest computational

cost in $\mathcal{O}(mn^2)$ [42, 43], where m and n are the numbers of rows and columns of the Hankel matrix.

4. Experiments

4.1 Numerical Simulation

A numerical simulation was conducted to quantitatively compare the performance of different reconstruction methods. 4-shot DWI images were generated by multiplying the 256×256 Shepp-Logan phantom with simulated smooth variation phase maps as shown in Figure 2(a), and then the 4-shot images were multiplied with eight coil sensitivity maps. Fourier transformation was performed to convert the images to k-space. And then, Gaussian noise with expectation $\mu = 0$ and standard deviation $\sigma = 0.01$ was added to each k-space.

To evaluate the performance of different reconstruction methods, we draw the error maps of the reconstructions according to the reference image.

4.2 *In Vivo* Experiments

The 8-shot head DWI were acquired on a Philips 3T Achieva TX MRI scanner (Philips Healthcare, Best, The Netherlands) equipped with an 8-channel head coil. The acquisition parameters were: TE/TR = 77/3000 ms, FOV = 232×232 mm^2, matrix size = 236×232, b-value = 800 s/mm^2, shot number = 8.

The 12-shot head DWI were acquired on United Imaging 3T uMR 790 scanner equipped with a 24-channel head coil. The acquisition parameters were: TE/TR = 62/3246 ms, FOV = 300×300 mm^2, matrix size = 224×224, b-value = 1000 s/mm^2, shot number = 12.

The human study was approved by the Institutional Review Board and written informed consent was obtained from the participants.

4.3 Image Reconstruction

Our results were compared with two state-of-the-art navigator-free DWI image reconstruction methods, including the POCS-ICE [11] and MUSSELS [12]. POCS-ICE alternatively estimates phase maps of different shots and DWI image. Both MUSSELS and the proposed method avoid calculating the phase variations of different shots and try to reconstruct multi-shot images, and then combine them to a single one by a square root of sum of squares. All sensitivity maps were estimated from non-diffusion-weighted data by eigenvalue based iterative self-consistent parallel imaging reconstruction [44].

In POCS-ICE reconstructions, the algorithm and the parameters used were identical to the original paper. In MUSSELS reconstructions, we utilized POCS-like algorithm share on [45], which is a time-saving implementation. The filter size in POCS-MUSSELS were set to 5×5, totally 25 pixels in the filter. And in POCS-like implementation of MUSSELS, another parameter, the number of rank is needed to be set. In our experiments, we tested different rank values, and then choose the best results. As in PLRHM, the circle radius R is set to 2, which means the total pixels of the filter is 13. The regularization parameter λ is set to 10. The tolerance of the simulation was set to 10^{-6} for simulation and 10^{-5} for *in vivo* data. The max iteration time is set to 200.

The relative l_2-norm error (RLNE) is exploited for quantitative analysis in numerical simulation. The RLNE is defined as

$$RLNE = \frac{\| \mathbf{x}_{ref} - \mathbf{x}_{rec} \|_2}{\| \mathbf{x}_{ref} \|_2} \tag{17}$$

where $\mathbf{x}_{ref}$ is the vectorized reference image, $\mathbf{x}_{rec}$ the vectorized reconstructed image.

All reconstruction algorithms were performed using MATLAB 2018b (Mathworks Inc., Natick, MA) on a personal computer with 3.30 GHz dual-core CPU and 16 GB RAM.

5. Results

5.1 Numerical Simulation

The results of simulation are shown in Figure 3. The direct reconstruction without any phase correction results in severe aliasing artifacts (Figure 4(e)). POCS-ICE removes most artifacts, but several artifacts still exist and can be seen in the image (Figure 4(b) and (f)). The reconstructions of POCS-MUSSELS (Figure 4(c)) and our method (Figure 4(d)) can recover image without obvious artifacts while there are smaller errors in our result which can be seen in the error maps (Figure 4(g) and (h)). The RLNE of POCS-ICE, POCS-MUSSELS and our method are 0.0263, 0.0334, and 0.0230, respectively. Thus, the proposed PLRHM leads to lowest reconstruction error on this simulated data.

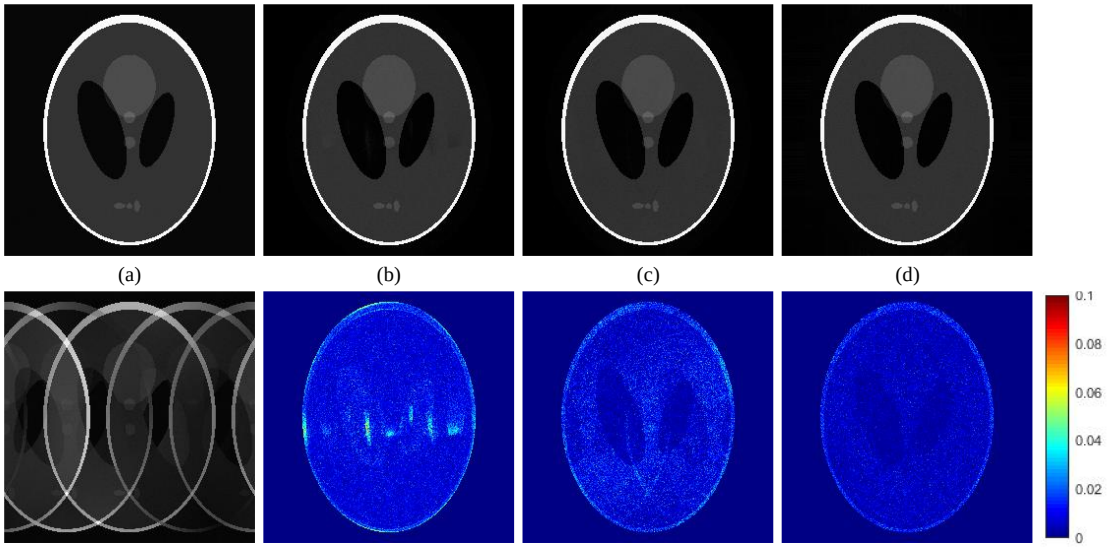

Figure 3. Reconstructed images of simulated Shepp-Logan phantom. (a) Reference (b) POCS-ICE, (c) POCS-MUSSELS, (d) the proposed method, (e) direct reconstruction without phase correction, (f)-(h) error map of (b)-(d).

5.2 *In Vivo* Experiments

For *in vivo* data, there is no golden standard for error maps calculation, thus we use a navigator-based method image reconstruction using image-space sampling function (IRIS) [8] to reconstruct an image as reference. Furthermore, the reconstruction results of *in vivo* data are one of number of signal averaged.

Figure 4 and Figure 5 show two slices reconstructions of 8-shot head DWI. Figure 4(d) and Figure 5(d) exhibit the references reconstructed by IRIS [8]. Slight artifacts still remain in the reconstructions of POCS-ICE (Figure 4(a) and Figure 5(a)), as marked by red arrows. POCS-MUSSELS reconstructions (Figure 4 (b) and Figure 5(b)) show no obvious artifacts but they look dark in the center of images, as marked by yellow arrows. While the proposed method (Figure 4(c) and Figure 5(c)) can effectively reconstruct the images with minimal artifacts. The reconstruction times for three methods are 152s, 548s and 2813s, respectively.

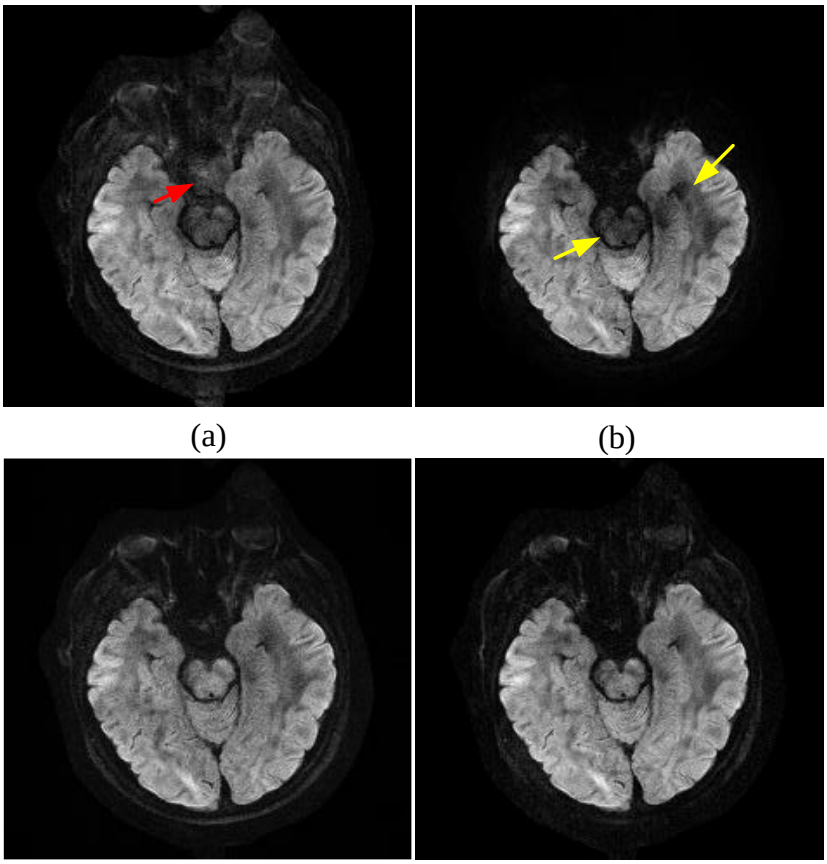

Figure 4. Reconstructions of slice 4 of 8-shot *in vivo* head DWI using different reconstruction methods. (a) POCS-ICE, (b) POCS-MUSSELS, (c) the proposed method, (d) reference reconstructed by IRIS. The residual artifacts are marked by the red arrow and the dark regions are marked by yellow arrows.

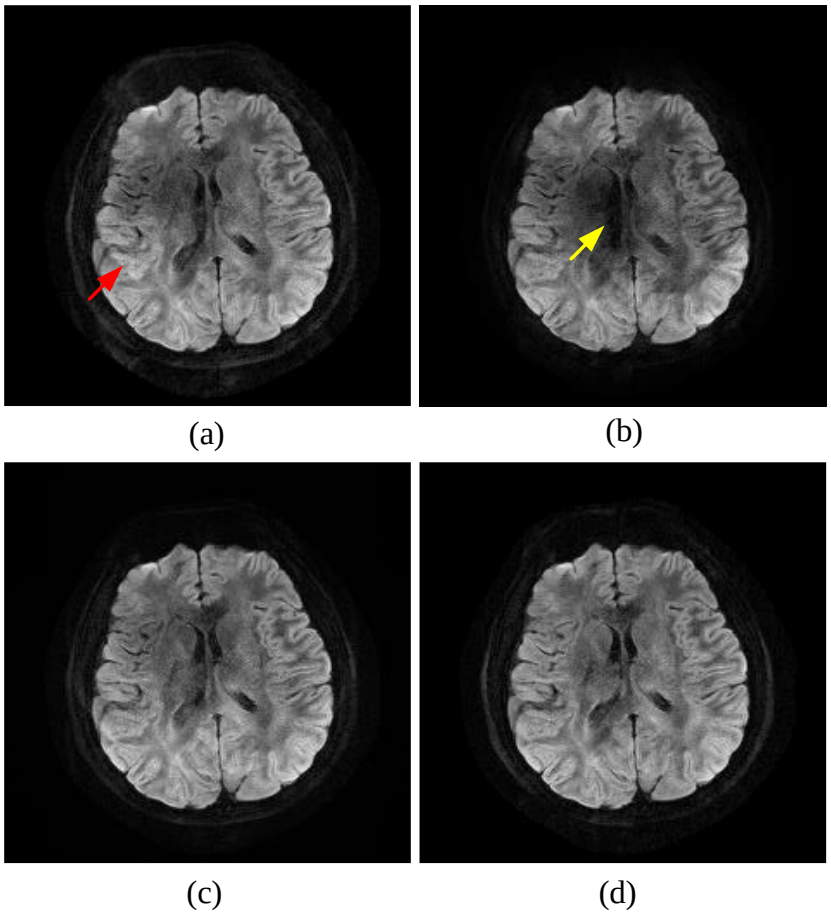

Figure 5. Reconstructions of slice 9 of 8-shot *in vivo* head DWI using different reconstruction methods. (a) POCS-ICE, (b) POCS-MUSSELS, (c) the proposed method, (d) reference reconstructed by IRIS. The residual artifact is marked by the red arrow and the dark region is marked by yellow arrow.

Figure 6 shows the reconstructions of 3 slices of 12-shot head DWI. Directly inverse Fourier transformation induces severe aliasing artifacts (Figure 6(a)). POCS-ICE fails to remove the severe aliasing artifacts (Figure 6(b)). POCS-MUSSELS removes the artifacts to some extent but slight artifacts still remain in the image(Figure 6(c)). While the proposed method can effectively reconstruct the image with minimal artifacts and shaper edges than POCS-MUSSELS, as shown in Figure 6(d). In this case, the shot number is up to 12, which is an aggressive high shot number for reconstruction. POCS-ICE and POCS-MUSSELS have difficulty to recover the artifact-free image, while the proposed method has the potential to handle the case with high number of shots. The reconstruction times for three methods are 336s, 1024s and 8856s, respectively.

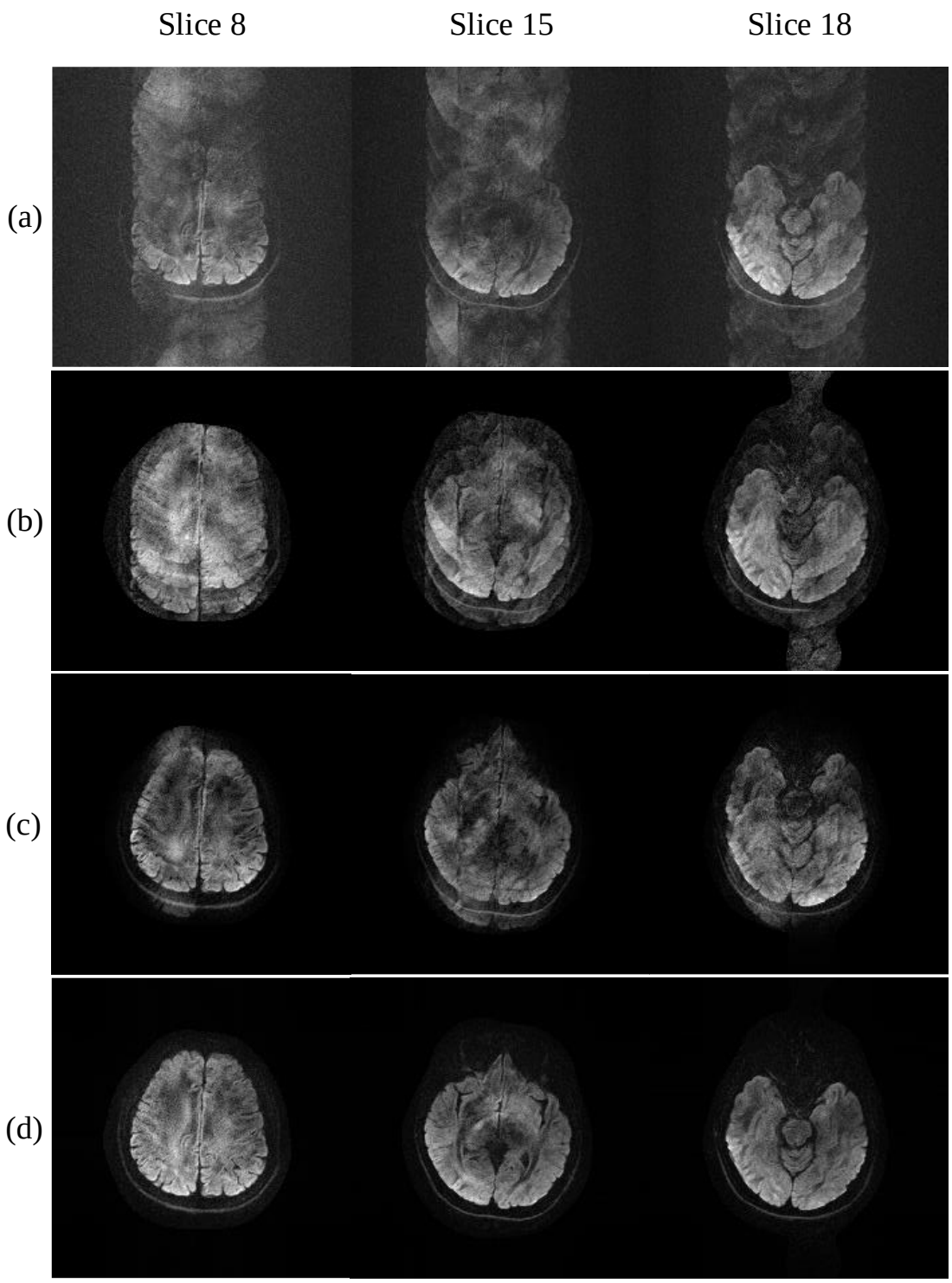

Figure 6. Reconstructions of 3 slices of 12-shot *in vivo* head DWI using different reconstruction methods. (a) direct reconstruction without correction, (b) POCS-ICE, (c) POCS-MUSSELS, (d) the proposed method.

6. Discussions

6.1 Discussion on the estimated rank

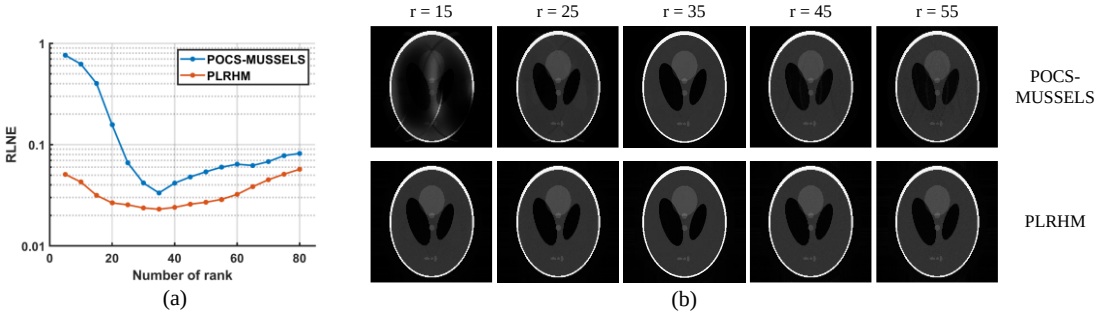

(a) (b)

Figure 7. The reconstructions of various rank values by POCS-MUSSELS and the proposed method. (a) The RLNE curve, (b) The reconstructions for different rank values.

The POCS-MUSSELS and the proposed method both have a parameter rank r to be set. While our method is less sensitive to the preset rank than POCS-MUSSELS arising from the experiments we have conducted. Figure 7 (a) shows the plots of RLNEs of different rank r of POCS-MUSSELS and our method on Shepp-Logan experiment. Both methods obtain the lowest RLNE value when the rank value is set to 35, while the RLNE value of our result is lower than POCS-MUSSELS. The plots show that low RLNE values can be obtained by choosing from a relatively wide range of rank values by using the proposed method. The reconstructions of various preset ranks by POCS-MUSSELS and the proposed method are shown in Figure 7 (b). Artifacts are stronger when the rank values are lower or higher than 35 in POCS-MUSSELS. While in the proposed method, the reconstructions are less sensitive to the preset rank and no obviously visible artifacts in the reconstructions.

It is still unknown how to theoretically choose an optimal rank. In practice, we observe that the proposed method has a good reconstruction performance within a range of rank values.

For the *in vivo* data, the extra navigator-echo signals, which share similar extra phase variations caused by subject motion with image-echo signals can be obtained by additionally acquiring central k-space in each shot. Therefore, we constructed the LORAKS **S**-matrix by the navigator-echo signals and then plotted the distribution of singular values of the Hankel matrix, as shown in Figure 8. The low-rankness can be observed from the singular values distribution, so as the Hankel matrix constructed by image-echo signals due to the similar phase variations.

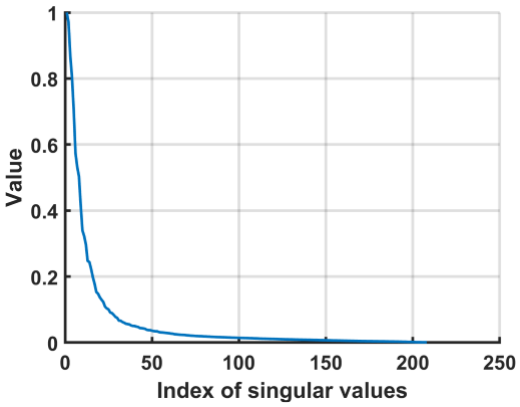

Figure 8. Singular values distribution of navigator signals.

Notice that the PSVT operator only constrains the rest $N-r$ singular values and keeps the previous r singular values unchanged in each iteration. We tested the reconstruction performances by using various rank values for 8-shot and 12-shot head DWI, and the results are shown in Figure 9 and Figure 10, respectively. For 8-shot and 12-shot DWI, the artifacts would still remain in the reconstructions where preset rank value is too low. When the rank is higher than 40, the reconstructions show noisier and slight artifacts occur which would degrade the image quality. Therefore, we would suggest setting the rank value between 10 to 40 for *in vivo* 8-shot and 12-shot data.

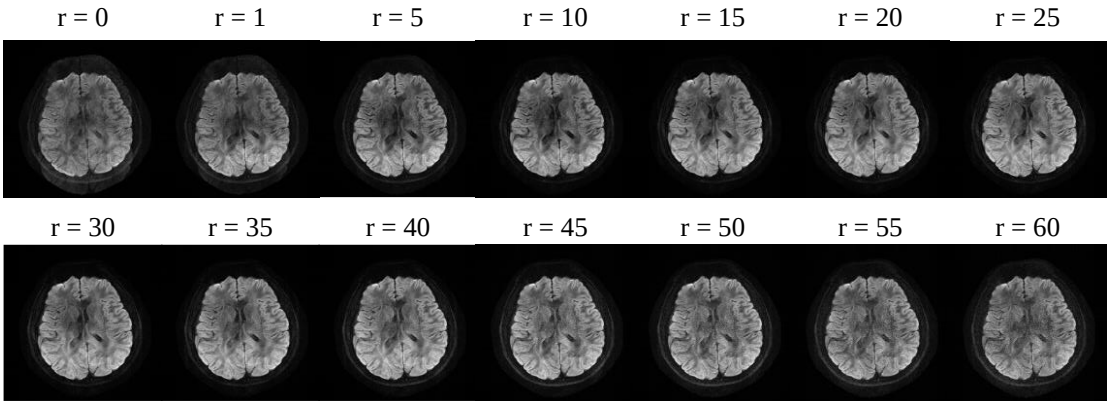

Figure 9. The reconstructions by various preset rank value in 8-shot DWI.

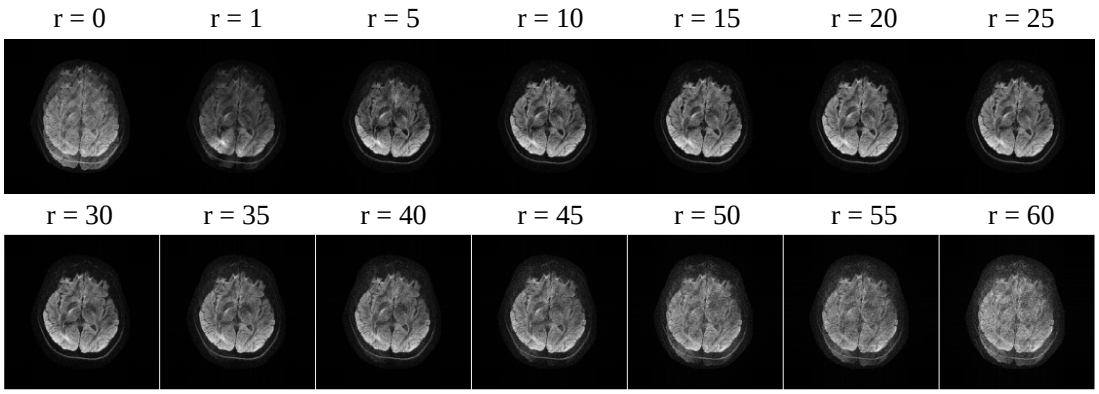

Figure 10. The reconstructions by various preset rank value in 12-shot DWI.

6.2 Discussion on empirical convergence

Despite theoretical convergence of ADMM for non-convex programming in Eq. (10) has not been proved yet, [39] has exploited the alternating scheme to solve the non-convex problem and have obtained promising results. We conducted extensive experiments and the algorithm converged finally in our experiments. Although the global optimal solution cannot be guaranteed, our experiments show that the convergence can be obtained empirically. Figure 11 (a) exhibits the empirical convergence of 8-shot *in vivo* head experiment. The difference is defined by $\| \mathbf{x}_{n+1} - \mathbf{x}_n \|_2^2 / \| \mathbf{x}_n \|_2^2$, corresponding to the relative difference between two iterations. Figure 11 (b) shows the results of representative iterations. There are no big improvements after 200 iterations, so we choose the max iterations to 200 in all experiments.

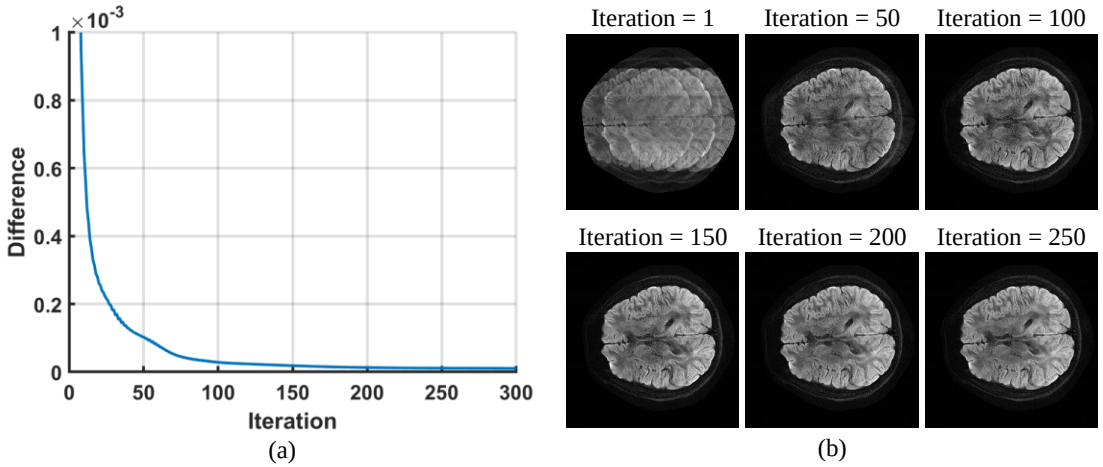

(a) (b)

Figure 11. The empirical convergence of ADMM algorithm. (a) The difference between two iterations, (b) results of representative iterations.

7. Conclusion

In this paper, we propose a method dubbed PLRHM to reconstruct magnetic resonance images in high-resolution multi-shot diffusion weighted imaging. This method enforces the low-rankness of Hankel matrix by exploiting the smooth phase property of multi-shot images. Then, we adopt the partial sum of singular values minimization strategy to enhance the low-rank constraint. The comparisons with the state-of-the-art navigator-free DWI reconstruction methods have shown that the advantage of PLRHM on better artifacts removal and high reconstruction quality. Furthermore, the proposed method has the potential to reconstruct high number of shots DWI image. One main disadvantage is that our method is time consuming and further we would like to research on reducing the reconstruction time.

Acknowledgments

This work was supported in part by National Key R&D Program of China (2017YFC0108700), National Natural Science Foundation of China (61971361, 61871341, 61811530021 and 61672335), Natural Science Foundation of Fujian Province of China (2018J06018), Fundamental Research Funds for the Central Universities (20720180056), Science and Technology Program of Xiamen (3502Z20183053), and China Scholarship Council.

The authors would like to thank Dr. Guobin Li in United Imaging Company for providing the 12-shot head DWI data in this paper.

References

[1] D. Le Bihan, E. Breton, D. Lallemand, P. Grenier, E. Cabanis, and M. Laval-Jeantet, "MR imaging of intravoxel incoherent motions: application to diffusion and perfusion in neurologic disorders," *Radiology,* vol. 161, no. 2, pp. 401-407, 1986.

[2] D. Le Bihan, J. F. Mangin, C. Poupon, C. A. Clark, S. Pappata, N. Molko, and H. Chabriat, "Diffusion tensor imaging: concepts and applications," *Journal of Magnetic Resonance Imaging,* vol. 13, no. 4, pp. 534-546, 2001.

[3] S. Mori and J. Zhang, "Principles of diffusion tensor imaging and its applications to basic neuroscience research," *Neuron,* vol. 51, no. 5, pp. 527-539, 2006.

[4] A. G. Sorensen, F. S. Buonanno, R. G. Gonzalez, L. H. Schwamm, M. H. Lev, F. R. Huang-Hellinger, T. G. Reese, R. M. Weisskoff, T. L. Davis, and N. Suwanwela, "Hyperacute stroke: evaluation with combined multisection diffusion-weighted and hemodynamically weighted echo-planar MR imaging," *Radiology,* vol. 199, no. 2, pp. 391-401, 1996.

[5] M. D. Budde and N. P. Skinner, "Diffusion MRI in acute nervous system injury," *Journal of Magnetic Resonance,* vol. 292, pp. 137-148, 2018.

[6] F. Farzaneh, S. J. Riederer, and N. J. Pelc, "Analysis of T2 limitations and off-resonance effects on spatial resolution and artifacts in echo-planar imaging," *Magnetic Resonance in Medicine,* vol. 14, no. 1, pp. 123-139, 1990.

[7] E. Solomon, N. Shemesh, and L. Frydman, "Diffusion weighted MRI by spatiotemporal encoding: analytical description and in vivo validations," *Journal of Magnetic Resonance,* vol. 232, pp. 76-86, 2013.

[8] H. K. Jeong, J. C. Gore, and A. W. Anderson, "High-resolution human diffusion tensor imaging using 2-D navigated multishot SENSE EPI at 7 T," *Magnetic Resonance in Medicine,* vol. 69, no. 3, pp. 793-802, 2013.

[9] X. Ma, Z. Zhang, E. Dai, and H. Guo, "Improved multi-shot diffusion imaging using GRAPPA with a compact kernel," *Neuroimage,* vol. 138, pp. 88-99, 2016.

[10] N. K. Chen, A. Guidon, H. C. Chang, and A. W. Song, "A robust multi-shot scan strategy for high-resolution diffusion weighted MRI enabled by multiplexed sensitivity-encoding (MUSE)," *Neuroimage,* vol. 72, no. 2, pp. 41-47, 2013.

[11] H. Guo, X. Ma, Z. Zhang, B. Zhang, C. Yuan, and F. Huang, "POCS‐enhanced inherent correction of motion‐induced phase errors (POCS‐ICE) for high‐resolution multishot diffusion MRI," *Magnetic Resonance in Medicine,* vol. 75, no. 1, pp. 169-180, 2016.

[12] M. Mani, M. Jacob, D. Kelley, and V. Magnotta, "Multi‐shot sensitivity‐encoded diffusion data recovery using structured low‐rank matrix completion (MUSSELS)," *Magnetic Resonance in Medicine,* vol. 78, no. 2, pp. 494-507, 2017.

[13] Y. Hu, E. G. Levine, Q. Tian, C. J. Moran, X. Wang, V. Taviani, S. S. Vasanawala, J. A. McNab, B. A. Daniel, and B. L. Hargreaves, "Motion‐robust reconstruction of multishot diffusion‐weighted images without phase estimation through locally low‐rank regularization," *Magnetic Resonance in Medicine,* vol. 81, no. 2, pp. 1181-1190, 2019.

[14] L. Guo, F. Huang, Z. Xu, Y. Mei, W. Fang, X. Ma, E. Dai, H. Guo, Q. Feng, and W. Chen, "eIRIS: Eigen-analysis approach for improved spine multi-shot diffusion MRI," *Magnetic Resonance Imaging,* vol. 50, pp. 134-140, 2018.

[15] W. Liu, X. Zhao, Y. Ma, X. Tang, and J.-H. Gao, "DWI using navigated interleaved multishot EPI with realigned GRAPPA reconstruction," *Magnetic Resonance in Medicine,* vol. 75, no. 1, pp. 280-286, 2016.

[16] E. Dai, Z. Zhang, X. Ma, Z. Dong, X. Li, Y. Xiong, C. Yuan, and H. Guo, "The effects of navigator distortion and noise level on interleaved EPI DWI reconstruction: a comparison between image‐and k‐space‐based method," *Magnetic Resonance in Medicine,* vol. 80, no. 5, pp. 2024-2032, 2018.

[17] K. P. Pruessmann, M. Weiger, M. B. Scheidegger, and P. Boesiger, "SENSE: sensitivity encoding for fast MRI," *Magnetic Resonance in Medicine,* vol. 42, no. 5, pp. 952-962, 1999.

[18] X. Zhang, D. Guo, Y. Huang, Y. Chen, L. Wang, F. Huang, and X. Qu, "Image reconstruction with low-rankness and self-consistency of k-space data in parallel MRI," *arXiv preprint arXiv:1909.02846,* 2019.

[19] J. P. Haldar, "Low-rank modeling of local k-space neighborhoods (LORAKS) for constrained MRI," *IEEE Transactions on Medical Imaging,* vol. 33, no. 3, pp. 668-681, 2013.

[20] K. H. Jin, D. Lee, and J. C. Ye, "A general framework for compressed sensing and parallel MRI using annihilating filter based low-rank Hankel matrix," *IEEE Transactions on Computational Imaging,* vol. 2, no. 4, pp. 480-495, 2016.

[21] G. Ongie and M. Jacob, "Off-the-grid recovery of piecewise constant images from few Fourier samples," *SIAM Journal on Imaging Sciences,* vol. 9, no. 3, pp. 1004-1041, 2016.

[22] F. Lam, C. Ma, B. Clifford, C. L. Johnson, and Z. P. Liang, "High‐resolution 1H‐MRSI of the brain using SPICE: data acquisition and image reconstruction," *Magnetic Resonance in Medicine,* vol. 76, no. 4, pp. 1059-1070, 2016.

[23] X. Qu, M. Mayzel, J. F. Cai, Z. Chen, and V. Orekhov, "Accelerated NMR spectroscopy with low‐rank reconstruction," *Angewandte Chemie International Edition,* vol. 54, no. 3, pp. 852-854, 2015.

[24] X. Qu, Y. Huang, H. Lu, T. Qiu, D. Guo, T. Agback, V. Orekhov, and Z. Chen, "Accelerated nuclear magnetic resonance spectroscopy with deep learning," *Angewandte Chemie International Edition,* DOI: 10.1002/anie.201908162, 2019.

[25] H. Lu, X. Zhang, T. Qiu, J. Yang, J. Ying, D. Guo, Z. Chen, and X. Qu, "Low rank enhanced matrix recovery of hybrid time and frequency data in fast magnetic resonance spectroscopy," *IEEE Transactions on Biomedical Engineering,* vol. 65, no. 4, pp. 809-820, 2017.

[26] J. Ying, H. Lu, Q. Wei, J.-F. Cai, D. Guo, J. Wu, Z. Chen, and X. Qu, "Hankel matrix nuclear norm regularized tensor completion for N-dimensional exponential signals," *IEEE Transactions on Signal Processing,* vol. 65, no. 14, pp. 3702-3717, 2017.

[27] J. Ying, J.-F. Cai, D. Guo, G. Tang, Z. Chen, and X. Qu, "Vandermonde factorization of Hankel matrix for complex exponential signal recovery—Application in fast NMR spectroscopy," *IEEE Transactions on Signal Processing,* vol. 66, no. 21, pp. 5520-5533, 2018.

[28] G. Ongie and M. Jacob, "Recovery of Piecewise Smooth Images from Few Fourier Samples," *In 2015 International Conference on Sampling Theory and Applications (SampTA),* pp. 543-547, 2015.

[29] P. J. Shin, P. E. Z. Larson, M. A. Ohliger, M. Elad, J. M. Pauly, D. B. Vigneron, and M. Lustig, "Calibrationless parallel imaging reconstruction based on structured low-rank matrix completion," *Magnetic Resonance in Medicine,* vol. 72, no. 4, pp. 959-970, 2014.

[30] J. P. Haldar and J. Zhuo, "P-LORAKS: Low-rank modeling of local k-space neighborhoods with parallel imaging data," *Magnetic Resonance in Medicine,* vol. 75, no. 4, pp. 1499-1514.

[31] T. H. Kim, K. Setsompop, and J. P. Haldar, "LORAKS makes better SENSE: Phase-constrained partial fourier SENSE reconstruction without phase calibration," *Magnetic Resonance in Medicine,* vol. 77, no. 3, pp. 1021-1035, 2017.

[32] Z.-P. Liang, "Spatiotemporal imaging with partially separable functions," in *2007 4th IEEE International Symposium on Biomedical Imaging: From Nano to Macro*, 2007, pp. 988-991: IEEE.

[33] B. Zhao, J. P. Haldar, A. G. Christodoulou, and Z.-P. Liang, "Image reconstruction from highly undersampled (k, t)-space data with joint partial separability and sparsity constraints," *IEEE Transactions on Medical Imaging,* vol. 31, no. 9, pp. 1809-1820, 2012.

[34] S. G. Lingala, Y. Hu, E. DiBella, and M. Jacob, "Accelerated dynamic MRI exploiting sparsity and low-rank structure: kt SLR," *IEEE Transactions on Medical Imaging,* vol. 30, no. 5, pp. 1042-1054, 2011.

[35] R. A. Lobos, T. H. Kim, W. S. Hoge, and J. P. Haldar, "Navigator-free EPI ghost correction with structured low-rank matrix models: New theory and methods," *IEEE Transactions on Medical Imaging,* vol. 37, no. 11, pp. 2390-2402, 2018.

[36] Z. Hu, X. Ma, T.-K. Truong, A. W. Song, and H. Guo, "Phase-updated regularized SENSE for navigator-free multishot diffusion imaging," *Magnetic Resonance in Medicine,* vol. 78, no. 1, pp. 172-181, 2017.

[37] B. Recht, M. Fazel, and P. A. Parrilo, "Guaranteed minimum-rank solutions of linear matrix equations via nuclear norm minimization," *SIAM review,* vol. 52, no. 3, pp. 471-501, 2010.

[38] Y. Hu, D. Zhang, J. Ye, X. Li, and X. He, "Fast and accurate matrix completion via truncated nuclear norm regularization," *IEEE Transactions on Pattern Analysis and Machine Intelligence,* vol. 35, no. 9, pp. 2117-2130, 2012.

[39] T.-H. Oh, H. Kim, Y.-W. Tai, J.-C. Bazin, and I. So Kweon, "Partial sum minimization of singular values in RPCA for low-level vision," in *Proceedings of the IEEE International Conference on Computer Vision*, 2013, pp. 145-152.

[40] S. Boyd, N. Parikh, E. Chu, B. Peleato, and J. Eckstein, "Distributed optimization and statistical learning via the alternating direction method of multipliers," *Foundations and Trends® in Machine learning,* vol. 3, no. 1, pp. 1-122, 2011.

[41] R. Chandra, S. Eisenstat, and M. Schultz, "Conjugate gradient methods for partial differential equations," Yale University New Haven, CT, 1978.

[42] T.-H. Oh, Y. Matsushita, Y.-W. Tai, and I. So Kweon, "Fast randomized singular value thresholding for nuclear norm minimization," in *Proceedings of the IEEE Conference on Computer Vision and Pattern Recognition*, 2015, pp. 4484-4493.

[43] G. H. Golub and C. F. Van Loan, "Matrix computations," *The Johns Hopkins University Press, Baltimore, USA,* 1989.

[44] M. Uecker, P. Lai, M. J. Murphy, P. Virtue, M. Elad, J. M. Pauly, S. S. Vasanawala, and M. Lustig, "ESPIRiT—an eigenvalue approach to autocalibrating parallel MRI: Where SENSE meets GRAPPA," *Magnetic Resonance in Medicine,* vol. 71, no. 3, pp. 990-1001, 2014.

[45] B. Bilgic, I. Chatnuntawech, M. K. Manhard, Q. Tian, C. Liao, S. S. Iyer, S. F. Cauley, S. Y. Huang, J. R. Polimeni, and L. L. Wald, "Highly accelerated multishot echo planar imaging through synergistic machine learning and joint reconstruction," *Magnetic Resonance in Medicine,* vol. 82, pp. 1343-1358, 2019.